ACS Catalysis

Research Article

Cite This: ACS Catal. 2019, 9, 7166–7178

pubs.acs.org/acscatalysis

Impact of Nanoparticle–Support Interactions in Co_3O_4/Al_2O_3 Catalysts for the Preferential Oxidation of Carbon Monoxide

Thulani M. Nyathi,[†] Nico Fischer,[†] Andrew P. E. York,[‡] David J. Morgan,[§] Graham J. Hutchings,[§] Emma K. Gibson,[∥,⊥] Peter P. Wells,[⊥,#,▽] C. Richard A. Catlow,[§,⊥,○] and Michael Claeys*[,†]

[†]Catalysis Institute and c*change (DST-NRF Centre of Excellence in Catalysis), Department of Chemical Engineering, University of Cape Town, Rondebosch 7701, South Africa

[‡]Johnson Matthey Technology Centre, Sonning Common, Reading, RG4 9NH United Kingdom

[§]Cardiff Catalysis Institute, Cardiff University, Main Building, Park Place, Cardiff, CF10 3AT, United Kingdom

[∥]School of Chemistry, Joseph Black Building, University of Glasgow, Glasgow G12 8QQ, United Kingdom

[⊥]UK Catalysis Hub, Research Complex at Harwell, Rutherford Appleton Laboratory, Harwell, Oxon OX11 0FA, United Kingdom

[#]School of Chemistry, University of Southampton, University Road, Southampton SO17 1BJ, United Kingdom

[▽]Harwell Science and Innovation Campus, Diamond Light Source Ltd., Chilton, Didcot OX11 0DE, United Kingdom

[○]Department of Chemistry, University College London, 20 Gordon Street, London, WC1H 0AJ, United Kingdom

Supporting Information

ABSTRACT: Different supporting procedures were followed to alter the nanoparticle–support interactions (NPSI) in two Co_3O_4/Al_2O_3 catalysts, prepared using the reverse micelle technique. The catalysts were tested in the dry preferential oxidation of carbon monoxide (CO-PrOx) while their phase stability was monitored using four complementary in situ techniques, viz., magnet-based characterization, PXRD, and combined XAS/DRIFTS, as well as quasi in situ XPS, respectively. The catalyst with weak NPSI achieved higher CO_2 yields and selectivities at temperatures below 225 °C compared to the sample with strong NPSI. However, relatively high degrees of reduction of Co_3O_4 to metallic Co were reached between 250 and 350 °C for the same catalyst. The presence of metallic Co led to the undesired formation of CH_4, reaching a yield of over 90% above 300 °C. The catalyst with strong NPSI formed very low amounts of metallic Co (less than 1%) and CH_4 (yield of up to 20%) even at 350 °C. When the temperature was decreased from 350 to 50 °C under the reaction gas, both catalysts were slightly reoxidized and gradually regained their CO oxidation activity, while the formation of CH_4 diminished. The present study shows a strong relationship between catalyst performance (i.e., activity and selectivity) and phase stability, both of which are affected by the strength of the NPSI. When using a metal oxide as the active CO-PrOx catalyst, it is important for it to have significant reduction resistance to avoid the formation of undesired products, e.g., CH_4. However, the metal oxide should also be reducible (especially on the surface) to allow for a complete conversion of CO to CO_2 via the Mars–van Krevelen mechanism.

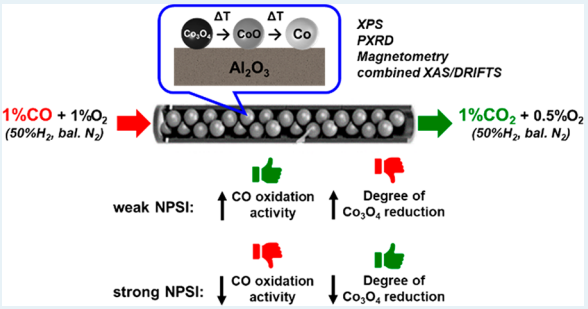

KEYWORDS: *CO-PrOx, Co_3O_4/Al_2O_3, nanoparticle–support interactions, catalyst performance, phase stability, in situ characterization*

1. INTRODUCTION

Heterogeneous catalysts commonly comprise metal or metal oxide nanoparticles anchored on mechanically and thermally stable carriers referred to as supports.[1] Most supports are either metal oxides (e.g., SiO_2 and Al_2O_3) or nonoxidic materials (e.g., graphite and SiC) with high mass-specific surface areas. High surface area is preferred as it allows for the uniform distribution of nanoparticles on the support and the deposition of relatively high amounts of the nanoparticles (or metal loadings), respectively.[1] The support material also helps prevent nanoparticle growth that may be induced by the high temperatures applied either during catalyst pretreatment/activation (e.g., calcination or reduction) and/or by the chemical environment of the catalyzed reaction.[2]

As a result of nanoparticle anchoring, certain properties of the nanoparticles (adsorption and reduction/oxidation capabilities) may be affected compared to their unsupported counterpart.[3] The method used to prepare the supported catalyst and the nature of the support material chosen also play a significant role in controlling the final properties of the

Received: February 16, 2019
Revised: June 24, 2019
Published: June 28, 2019

Table 1. Composition of the Reverse Micelle Solutions Prepared To Obtain CAT 1 and CAT2

sample name	*n*-hexane (g)	PEGDE (g)	H_2O (g)	o/s[a] (mol/mol)	w/s[b] (ω, mol/mol)	$Co(NO_3)_2{\cdot}6H_2O$ (g)
CAT 1	875.0	161.0	12.0	25.6	1.7	1.3
CAT 2	500.0	68.4	26.4	34.5	8.7	2.6

[a]Oil-to-surfactant molar ratio. [b]Water-to-surfactant molar ratio.

nanoparticles.[4,5] In general, very strong nanoparticle−support interactions (NPSI) between an oxidic support and oxide nanoparticles usually cause the reduction of the nanoparticles to be difficult.[6−8] For example, the conventional impregnation of irreducible supports like SiO_2 and Al_2O_3 with an aqueous solution of cobalt nitrate results in Co_3O_4-based catalysts that are relatively hard to reduce to metallic Co in a H_2 environment. On the other hand, on reducible supports like CeO_2 and ZrO_2, the reduction of Co_3O_4 is thermally less demanding but is still relatively difficult when compared to the reduction of unsupported Co_3O_4.[6,8]

We have previously conducted an in situ study investigating the effect of the crystallite size of Al_2O_3-supported Co_3O_4 nanoparticles on the preferential oxidation of CO (CO-PrOx) in a H_2-rich gas mixture.[9] CO-PrOx is a promising final step for the removal of trace amounts of CO in H_2-rich streams (e.g., originating from the consecutive CH_4 steam reforming and the water−gas shift processes) before being fed into proton exchange membrane fuel cells (PEMFCs) for power generation, as the CO poisons the Pt-based anode catalyst of PEMFCs.[10−12] We were able to show that Co_3O_4 reduces to CoO and ultimately to metallic Co at high reaction temperatures and that the reduction is influenced by crystallite size. This catalyst phase change proved to be unfavorable as less CO_2 was formed, and instead, CH_4 was produced due to the presence of the metallic Co. Co_3O_4 or specifically the Co^{3+}−Co^{2+} redox pair is believed to play an important role in the oxidation of CO.[13−16]

After observing the phase transformations, we speculated that introducing strong NPSI into the Co_3O_4/Al_2O_3 system would limit the reduction of Co_3O_4 and widen the temperature window for the CO-PrOx reaction. In our previous study,[9] the reverse micelle technique was used to prepare unsupported Co_3O_4 nanoparticles of varying sizes. The Al_2O_3 support was only contacted with the Co_3O_4 nanoparticles after their calcination.[9,17] This way, the strength of the interaction between the support and the nanoparticles could be minimized to allow for the exclusive study of crystallite size effects. However, in the present study, two of the four different supporting methods detailed by Fischer et al.[5] to alter the NPSI were explored. Their approach involved contacting the Al_2O_3 support with each of the cobalt species [e.g., $Co(NO_3)_2$, $Co(OH)_x$ or Co_3O_4, respectively] formed during the different stages of the reverse micelle technique or during catalyst pretreatment. Therefore, the uniqueness of our work is in how we have manipulated the interaction between the Co_3O_4 nanoparticles and the Al_2O_3 support to influence the activity and phase stability of Co_3O_4 during CO-PrOx. To the best of our knowledge, such a study has not been done before in the context of CO-PrOx.

The prepared Co_3O_4/Al_2O_3 catalysts were then tested under "dry" CO-PrOx conditions (i.e., with no H_2O and CO_2 present in the feed) and characterized using four complementary in situ techniques, viz., powder X-ray diffraction (PXRD), magnetometry, and combined X-ray absorption spectroscopy (XAS) and diffuse reflectance infrared Fourier-transform spectroscopy (DRIFTS). PXRD, magnetometry, and XAS are bulk-sensitive techniques that were used to study the phase changes of the Co_3O_4/Al_2O_3 catalysts, and DRIFTS is a surface-sensitive technique used for the detection of adsorbed and gas-phase reaction species as a function of temperature and time. Lastly, quasi-in-situ X-ray photoelectron spectroscopy (XPS) was carried out to study the nature of the surface of each catalyst at selected reaction temperatures.

2. METHODS

2.1. Catalyst Preparation. Two supported catalysts were prepared using the reverse micelle technique, but the method of supporting the nanoparticles was varied in each case. Each of the two variations have been described in detail by Fischer et al.[5] The catalysts were named CAT 1 and CAT 2 to distinguish between the variations made for the support. See Table 1 for the composition of the reverse micelle solutions.

To prepare CAT 1, an aqueous solution containing $Co(NO_3)_2{\cdot}6H_2O$ (Sigma-Aldrich, reagent grade 98% purity) was added to a stirring mixture of *n*-hexane (AR grade, Kimix) and the nonionic surfactant pentaethylene glycol dodecylether (PEGDE) (Akzo Nobel) at room temperature and atmospheric pressure. Thereafter, aqueous NH_3 (25 wt %, Kimix) at a 1:4 Co^{2+}:NH_3 molar ratio was added to the prepared reverse micelle solution to initiate the precipitation process, followed by the dropwise addition of acetone (AR grade, Kimix) to destabilize the reverse micelles and liberate the green precipitate [most likely $Co(OH)_x$]. Acetone was further used to wash the precipitate and rid it of excess surfactant. The precipitate was allowed to settle and then the supernatant was decanted through siphoning. The precipitate was dried and calcined at 120 and 200 °C, respectively. The obtained Co_3O_4 powder was redispersed in distilled water under ultrasonication at room temperature and atmospheric pressure for 60 min, and thereafter, the suspension was transferred to a preweighed dry powder of Al_2O_3 (PURALOX, SCCa 5/150, Sasol Germany GmbH: S_{BET} = 162 m^2/g, V_{pore} = 0.47 cm^3/g, d_{pore} = 11.5 nm, $d_{particle}$ = 150−200 μm) in order to achieve a loading of 10 wt % Co_3O_4. The water was evaporated under reduced pressure in a rotary evaporator.

Unlike in the preparation of CAT 1, obtaining CAT 2 involved the addition of the Al_2O_3 support after the precipitation with NH_3 (but before the addition of acetone). The slurry was stirred for 60 min. After extensive washing of the solid with acetone, a green [$Co(OH)_x$] precipitate together with the reddish-pink impregnated Al_2O_3 support was obtained. The impregnated support was much denser than the precipitate and, therefore, was separated using a separating funnel. The precipitate not taken up by the support was not redispersed and deposited onto the already impregnated support, as this would have resulted in nanoparticles with different interactions with the support within the same sample. However, by not depositing the precipitate, the targeted 10 wt % Co_3O_4 loading was not achieved. Nonetheless, the impregnated support was dried and calcined at 120 and 400 °C, respectively. The composition of the reverse micelle

DOI: 10.1021/acscatal.9b00685
ACS Catal. 2019, 9, 7166−7178

solutions and the subsequent drying and calcination conditions used were to ensure that the Co_3O_4 crystallites in CAT 1 and CAT 2 have similar starting average sizes[5] (see also section 3.1).

2.2. Catalyst Characterization. Powder X-ray diffraction (PXRD) was performed in a Bruker D8 Advance X-ray diffractometer equipped with a cobalt source ($\lambda_{K\alpha1}$ = 1.788 97 Å) and a position-sensitive detector (Bruker Vantec). For all samples, the optics were set to parallel beam geometry. A 2θ range of 20°−120°, step size of 0.043°, and a time per step of 0.75 s were used, giving a scan time of 29 min, 50 s. All recorded diffraction patterns were compared to known diffraction patterns from the International Centre for Diffraction Data PDF-2 database[18] to determine the species present. To further identify phases and obtain the average crystallite size, Rietveld refinement utilizing the software package Topas 4.2[19] was carried out. As the alumina support material used in this study is known to be present as mixed phases of γ-Al_2O_3 and δ-Al_2O_3 and as the crystal structure of δ-Al_2O_3 is not known at this stage, an approach for partial or not known crystal structures (PONKCS), first described by Scarlett and Madsen,[20] was used.

Transmission electron microscopy (TEM) was performed for each sample using a Tecnai F20 transmission electron microscope operated at 200 kV with a field emission gun. The obtained micrographs were analyzed using the freeware ImageJ[21] in order to ultimately obtain average particle sizes and size distributions. The Co_3O_4 loading was determined by energy-dispersive X-ray (EDX) spectroscopy using a LEO 1450 SEM/EDX instrument.

The reducibility of the individual catalysts was assessed by hydrogen temperature-programmed reduction (H_2-TPR) performed in a Micromeritics AutoChem 2910 instrument equipped with a thermal conductivity detector (TCD). A 0.1 g portion of freshly prepared supported catalyst was loaded in a U-tube quartz reactor and heated from 60 to 920 °C using a 10 °C/min ramp rate in a flow of 5 vol % H_2 in Ar [50 mL (NTP)/min].

2.3. In Situ Catalyst Characterization and Testing.

2.3.1. Quasi-in-Situ X-ray Photoelectron Spectroscopy. X-ray photoelectron spectroscopy (XPS) measurements were performed on a Kratos Axis Ultra DLD photoelectron spectrometer utilizing monochromatic Al radiation (1486.6 eV photon energy) at the Cardiff Catalysis Institute (part of Cardiff University, Wales, UK). All data were acquired at a pass energy and step size of 40 and 0.1 eV, respectively, for high-resolution spectra and 160 and 1 eV, respectively, for survey scans. Charge compensation was achieved using the Kratos immersion lens system, and all spectra were subsequently calibrated to the C(1s) line taken to be 284.8 eV.

For the quasi-in-situ H_2-TPR and CO-PrOx experiments, the samples were first pressed in to disks and placed in a gold-plated cup before placement into a Kratos catalysis cell and evacuation to a vacuum of ca. 10^{-7} mbar. Pure H_2 or the CO-PrOx feed mixture (0.9% CO, 0.9% O_2, 50% H_2, 40% N_2, and 8.2% Ar), respectively, was then flowed through the cell, controlled with a mass flow controller. The amount of CAT 1 and CAT 2 used was 0.5 g and the total gas flow was 50 and 30 mL (NTP)/min, respectively, to maintain a constant GHSV of 60 000 mL/$g_{Co_3O_4}$·h. The samples were heated using a PBN heater under gas flow from 50 °C to the desired temperature, which was held for 1 h. Reaction quenching was achieved by swapping to Ar to purge the system and cooling down under this stream. Where there was a mixture of chemical phases after a heat treatment, their relative concentrations were calculated using CasaXPS (v2.3.17 PR1.1) after removal of a Shirley background and applying sensitivity factors from the manufacturer. Line shapes used for fitting the Co($2p_{3/2}$) region were derived from standard materials.

2.3.2. In Situ Magnetometry and PXRD Studies. A low-frequency vibrating sample magnetometer[22,23] with a maximum field strength of 2 T [developed at the University of Cape Town (UCT), South Africa, in collaboration with Sasol Ltd., South Africa] and a UCT-developed PXRD capillary cell[23−25] mounted on a Bruker D8 Advance Laboratory X-ray diffractometer equipped with a molybdenum source ($\lambda_{K\alpha1}$ = 0.7093 Å) were used for the catalyst-testing experiments. The optics of the diffractometer were set to parallel beam geometry to minimize possible peak shifts due to sample height differences (sample displacement). The magnetometer was specifically designed for the detection of ferromagnetic and superparamagnetic materials. In the present study, this is only metallic Co,[26] as Co_3O_4[27] and CoO[28] are antiferromagnetic (see Supporting Information for the definitions of ferromagnetism, superparamagnetism, and antiferromagnetism). On the other hand, the PXRD can detect the crystalline phases Co_3O_4, CoO, and Co up to the intrinsic instrument limitations regarding crystallite size and concentration.

During catalyst testing in the magnetometer, the temperature was held for 60 min at every 25 °C between 50 and 350 °C during heating and cooling at a rate of 1 °C/min while magnetization measurements were taken at a field strength of 2 T every 10 min. The data from these measurements and those from a previously performed calibration of a 0.1 g of freshly reduced metallic cobalt sample enabled the calculation of the degree of reduction, defined as the amount of metallic cobalt formed relative to the amount of cobalt in the starting material Co_3O_4 (see Figure S1 as well as equations S1 and S2 in the Supporting Information). Similarly, PXRD patterns were also recorded during the 60 min holding time every 10 min. A 2θ range of 15°−30°, a step size of 0.019°, and a time per step of 0.2 s (giving a scan time of 4 min 2 s) were chosen for each scan.

Both instruments are based on a single fixed bed reactor and for the experiments performed in each instrument, the gas composition and the gas-hourly space velocity (60 000 mL/$g_{Co_3O_4}$·h) were kept constant. The reaction mixture composed of 0.9% CO, 0.9% O_2, 52.1% H_2, and balance N_2. We note that the amount of O_2 added is in excess of the stoichiometric amount by a factor of 2 to ensure complete conversion of CO to CO_2. The use of a stoichiometric amount of O_2 and other O_2:CO ratios will be the focus in a future publication(s). Also, the gases CO_2 and H_2O were not co-fed, as the study aimed to investigate the sole effect of H_2 on the catalytic performance and reduction of Co_3O_4. The presence of CO_2 and H_2O may mask this effect. However, the effect of both H_2O and CO_2 will also be a topic in a future publication(s). The amount of the supported catalyst loaded into the magnetometer reactor was 1.1 g for CAT 1 and 1.7 g for CAT 2 to compensate for the slight differences in the Co_3O_4 loadings (see the EDX results in Table 2), and the gas flow rate was kept at 100 mL (NTP)/min. The mass of catalyst loaded into the PXRD capillary cell reactor was 0.015 g with the gas flow rate of 1.4 mL (NTP)/min for CAT 1 and 0.9 mL (NTP)/min for CAT 2.

DOI: 10.1021/acscatal.9b00685
ACS Catal. 2019, 9, 7166−7178

The products were analyzed using an Agilent Technologies 490 micro-GC fitted with three analysis modules equipped with thermal conductivity detectors for detecting CO, O_2, H_2, CO_2, CH_4, and N_2. Two molecular sieve 5 Å PLOT columns of 10 and 20 m lengths were employed to separate the gases. In the shorter column, Ar was chosen as the carrier gas to allow for the detection of H_2, while H_2 was chosen as the carrier gas in the 20 m column separating O_2, N_2, CH_4, and CO. The third column was a 10 m PoraPlot Q column with H_2 as the carrier gas and was mainly used for the separation and detection of CO_2. The reactor outlet gas was injected into the micro-GC every 5 min throughout performed reaction experiments. We note that the conversion of H_2 was too low to be accurately measured because of the low amounts of O_2 (for H_2O formation) and CO (for CH_4 and H_2O formation) that were fed.

2.3.3. Combined in Situ XAS/DRIFTS Studies. XAS measurements were performed at the Co K-edge (7709 eV) on the B18 beamline at the Diamond Light Source (session SP16006-1), Didcot, UK. Measurements were performed in transmission mode using a QEXAFS setup with fast-scanning Si(111) double crystal monochromators for the Co edge. The time resolution of the spectra reported herein was 95.53 s/spectrum (k_{max} = 14.8). A DaVinci arm fitted with Praying Mantis Optics was used to refocus the IR beam outside the FTIR spectrometer so that the X-ray beam could be transmitted through the DRIFTS cell. The samples were placed in a previously reported Harrick X-ray transmission DRIFTS cell attached to the end of the DaVinci arm.[29−31] The XAS/DRIFTS cell has an X-ray path length of 3.17 mm placed 1.04 mm below the surface of the catalyst. DRIFTS spectra were collected with an Agilent Carey 680 FTIR spectrometer taking one scan every minute with a resolution of 4 cm^{-1} using the liquid nitrogen cooled MCT detector.

Each sample was heated from room temperature to 100 °C at a rate of 10 °C/min in helium, which was then replaced with the reaction gas (0.9% CO, 0.9% O_2, 52.1% H_2, and balance N_2) at a flow rate of 4.7 mL (NTP)/min for 0.05 g of CAT 1 and 2.9 mL (NTP)/min for 0.05 g of CAT 2. Upon reaching 100 °C, both XAS and DRIFTS spectra were recorded over a 1 h duration. Thereafter, the temperature was changed using a ramp rate of 1 °C/min and held every 25 °C for 1 h until reaching a maximum temperature of 350 °C. The cell was cooled back down to 100 °C in a similar stepwise fashion under the reacting gas as in the heating ramp. XAS/DRIFTS measurements were taken continuously throughout each experiment.

For EXAFS (extended X-ray absorption fine structure) analysis, all spectra were acquired concurrently with the Co foil placed between I_t and I_{ref}. The data processing was performed using IFEFFIT with the Horae package (Athena and Artemis).[32,33] The amplitude reduction factor, S_0^2, was derived from EXAFS data analysis of the Co foil.

3. RESULTS AND DISCUSSION

3.1. Ex Situ TEM, PXRD, and EDX Analysis. For the various supporting procedures followed, it was important to keep the size of the cobalt oxide crystallites in the two catalysts within a similar narrow size range. This was to allow for the effect(s) of the NPSI during CO-PrOx to be studied excluding any size effects. Fischer et al.[5] observed that the supporting procedure followed to obtain CAT 2 results in Co_3O_4 nanoparticles with a size between 3 and 4 nm, even when the impregnated support was calcined at 400 °C. On the other hand, the method used to obtain CAT 1 allows for more flexibility, as sizes larger than 4 nm can potentially be obtained. This is because the support is only contacted with the calcined Co_3O_4 nanoparticles at a later stage in the overall synthesis, and in doing so, the crystallite size remains unchanged.[9,17] Furthermore, the size of the nanoparticles in CAT 1 is mostly determined by the composition of the reverse micelle solution, i.e., the oil/water-to-surfactant ratio and the amount of $Co(NO_3)_2{\cdot}6H_2O$ used. Therefore, the average size of the Co_3O_4 nanoparticles was set to vary within the narrow range of 3−5 nm, which was achieved by applying a low water to surfactant ratio in the reverse micelle system, especially in the case of CAT 1 (Table 1).

TEM analysis was used to obtain size distributions and to determine the average size of the Co_3O_4 particles. It should be noted that the images in Figure 1A,B give a relatively poor

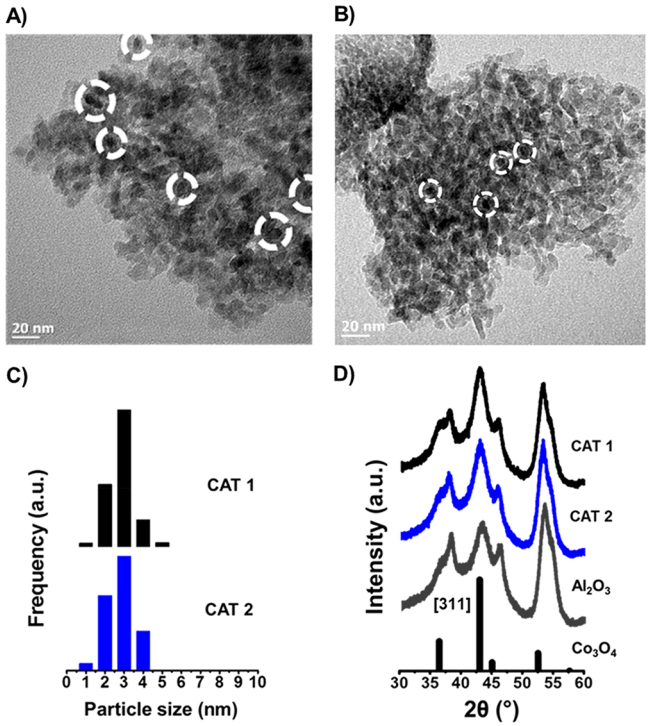

Figure 1. TEM images of (A) CAT 1 and (B) CAT 2, as well as the derived (C) particle size distributions. The white dashed circles show some of the identified Co_3O_4 particles. (D) Recorded PXRD patterns of CAT 1, CAT 2, and the bare Al_2O_3 support (radiation source: Co Kα1 = 1.788 97 Å). Also included is the reference diffraction lines of Co_3O_4 (ICDD card no.: 01-073-1701).

contrast between the Co_3O_4 particles and those of the Al_2O_3 support; however, number-based particle size distributions could still be derived and are shown in Figure 1C. The presence of Co_3O_4 in each catalyst was confirmed with PXRD (Figure 1D), which also yielded the average volume-based crystallite size. The 2θ range of the PXRD patterns shown in Figure 1D highlights the differences between the two supported catalysts and the bare support. As the average crystallite sizes for each catalyst are below 5 nm, the reflections due to Co_3O_4 are low in intensity and are partially overlapping with those of the Al_2O_3, especially the [311] reflections at 43° of both phases. However, the presence of Co_3O_4 in CAT 1 and CAT 2 was ultimately confirmed by the apparent increase in

DOI: 10.1021/acscatal.9b00685
ACS Catal. 2019, 9, 7166−7178

Table 2. PXRD- and TEM-Derived Average Co_3O_4 Crystallite Sizes for CAT 1 and CAT 2, as Well as the EDX-Derived Co_3O_4 Loadings.

sample name	av Co_3O_4 crystallite sizes (nm)			EDX Co_3O_4 loading (wt %)
	PXRD[a]	TEM[b]	TEM[c]	
CAT 1	4.5	3.3 ± 0.6	3.7 ± 0.7	9.4
CAT 2	3.8	3.2 ± 0.8	3.9 ± 0.9	5.9

[a]Volume-based average crystallite size obtained by Rietveld refinement with Topas 4.2. [b]TEM number-based average crystallite sizes and standard deviations calculated by $\bar{d}_{c,n} = \sum_{i=1}^{N} n_i d_i / N$ and $\sigma_n = \sqrt{\sum_{i=1}^{N} (d_i - \bar{d}_{c,n})^2 / N - 1}$. [c]TEM volume-based average crystallite sizes and standard deviations calculated by $\bar{d}_{c,v} = \sum_{i=1}^{N} n_i d_i^4 / \sum_{i=1}^{N} n_i d_i^3$ and $\sigma_v = \sqrt{\sum_{i=1}^{N} n_i d_i^3 (d_i - \bar{d}_{c,v})^2 / \frac{N-1}{N} \sum_{i=1}^{N} n_i d_i^3}$, where N is the total number of particles counted, d_i is the length of particle i, and n_i is the number of particles with the size d_i.

the intensity of the [311] reflection relative to the [400] reflection of Al_2O_3 at 53.7°.

Summarized in Table 2 are the PXRD- and TEM-derived volume- and number-based average crystallite sizes, respectively. The volume-based sizes from PXRD and TEM are in very good agreement, and similar sizes for both catalysts were obtained, even though different supporting procedures were followed. For the full recorded PXRD scans of the catalysts and the support, as well as the fits obtained after carrying out Rietveld refinement, see Figure S2 (SI). Table 2 also shows the EDX-derived Co_3O_4 loading for the different supported catalysts, and Figure S3 (SI) shows the size of the different regions of each sample that were scanned for the detection of Co, O, and Al. The loading targeted in each sample was 10 wt %. The method for preparing CAT 2 did not allow for the complete uptake of $Co(OH)_x$ by the Al_2O_3 support, as already mentioned in section 2.1.

3.2. H_2-TPR and Quasi-in-Situ XPS Studies. The success of the different supporting methods in altering the strength of the NPSI was first assessed using H_2-TPR. Figure 2 shows the

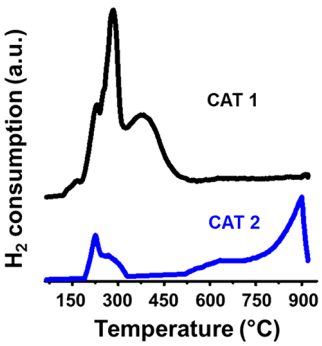

Figure 2. H_2-TPR profiles of CAT 1 and CAT 2.

H_2-TPR profiles of CAT 1 and CAT 2. The Co_3O_4 particles in CAT 1 reduce below 500 °C in multiple reduction steps. The particles in CAT 2 display two reduction peaks in the temperature range of 180−350 °C and a separate peak above 750 °C. Others have also observed similar reduction behavior for Al_2O_3-supported Co_3O_4 catalysts as that seen for CAT 2.[5−7] The two low-temperature peaks are generally assigned to the reduction of weakly bound Co_3O_4 possibly forming CoO and metallic Co. The high-temperature peak above 750 °C can be assigned to the reduction of strongly bound CoO_x species or cobalt aluminate-like species ($Co_xAl_yO_z$).

In the synthesis of CAT 2, some Co^{2+} ions of the precursor may have reacted with some of the Al_2O_3 support to form these hard-to-reduce species during calcination.[5] Alternatively, these species could also be formed during the H_2-TPR experiment due to the presence of the reduction product H_2O.[34] As the temperatures are increased, the Co^{3+} ions of Co_3O_4 are reduced to Co^{2+} ions and some of these ions could then react with the support. CAT 1 was prepared from contacting dispersed, precalcined Co_3O_4 particles with the Al_2O_3 support, which consequently minimized the interaction between the particles and the support.[5]

Quasi-in-situ XPS analysis was performed during H_2-TPR studying the surface composition of each catalyst after their low-temperature reduction. As observed from the H_2-TPR results (Figure 2), CAT 1 showed most of its reduction activity below 500 °C, while CAT 2 displayed reduction behavior below and above this temperature. Figure 3 shows the recorded Co 2p core-level spectra of CAT 1 and CAT 2 in their oxidic states and after exposure to H_2 at 500 °C. The position of the Co $2p_{3/2}$ peak in the spectra of the fresh samples is at 779.7 and 780.4 eV, respectively, in excellent agreement with values reported in the literature for pure Co_3O_4.[13,16,35,36] After treatment in H_2, CAT 1 shows the presence of Co^{2+} in the form of CoO (781.5 eV) and metallic Co (778.3 eV), respectively, at a ratio of 45:55, while CAT 2 had a $CoO:Co^0$ ratio of 78:22.

The results obtained for both catalysts indicate that Co_3O_4 was not completely converted to metallic Co. In contrast, during conventional H_2-TPR (Figure 2), CAT 1 showed no (or little) reduction behavior above 500 °C, which implied almost complete reduction of this catalyst. However, it should be noted that the design of the cell used for the quasi-in-situ experiments is a "flow-over" system where the gas mostly passes over the pressed/pelleted sample and does not penetrate deep into it. On the other hand, the U-tube reactor used for conventional H_2-TPR is a "flow-through" system where the gas does flow through the packed catalyst bed. These differences in hydrodynamics could explain the slight disagreement in the reduction results obtained (especially for CAT 1). Nevertheless, it is evident that CAT 2 possesses much stronger NPSI compared to CAT 1.

3.3. In Situ Catalyst Characterization and Testing: Magnetometry, PXRD, XPS, and Combined XAS/DRIFTS Studies. *3.3.1. PXRD, Magnetometry, and XPS.* Catalyst testing was performed in a fixed-bed reactor under dry CO-PrOx conditions (i.e., in the absence of H_2O and CO_2) and coupled with in situ characterization using the previously mentioned magnetometer[22,23] and PXRD capillary cell.[23−25] Figures 4 and 5 show the magnetometry and PXRD data as well as the calculated average outlet gas flow rates of CO, O_2, CO_2, and CH_4 as a function of temperature for CAT 1 and CAT 2. We note that the chosen presentation of the catalytic data as shown in Figures 4 and 5 gives a clearer picture of the different reactions taking place (viz., CO oxidation to CO_2, H_2 oxidation to H_2O (through the conversion of O_2), and CO hydrogenation to CH_4) by showing the changing concentrations of all gases being detected at the reactor outlet. However, the CO_2 yield, O_2 selectivity to CO_2, and CH_4 yield are presented in Figures S4, S5, and S6, respectively, in the

DOI: 10.1021/acscatal.9b00685
ACS Catal. 2019, 9, 7166−7178

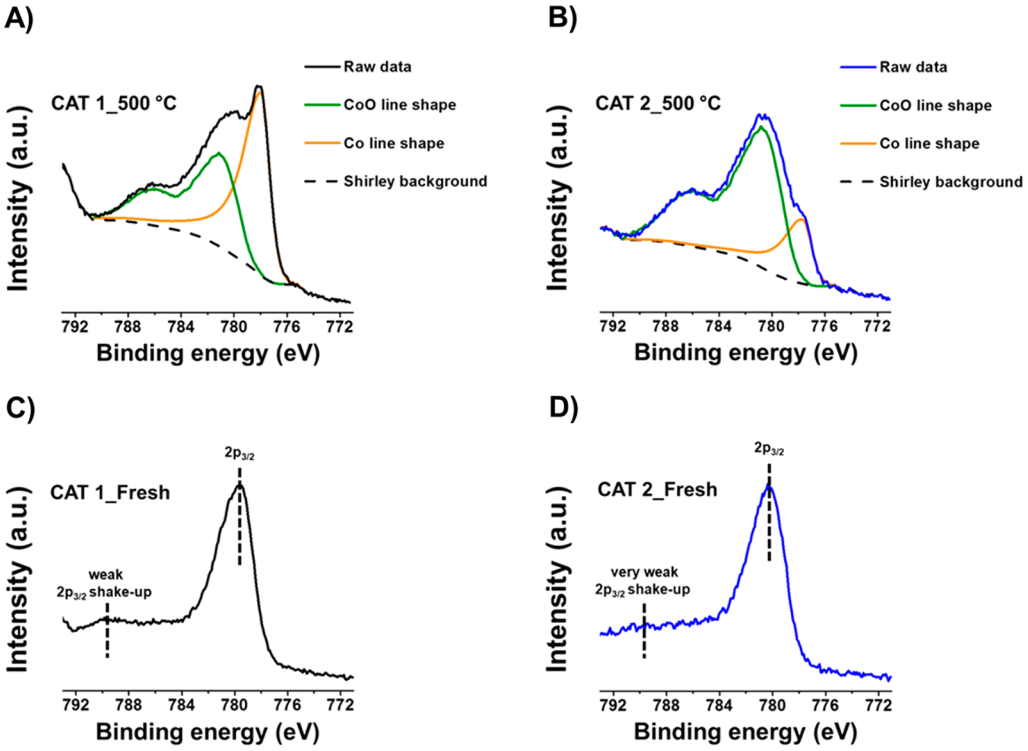

Figure 3. Recorded Co 2p core level spectra of (A) CAT 1 and (B) CAT 2, after being treated at 500 °C in pure H_2, together with spectra for their fresh unreduced state (panels C and D, respectively).

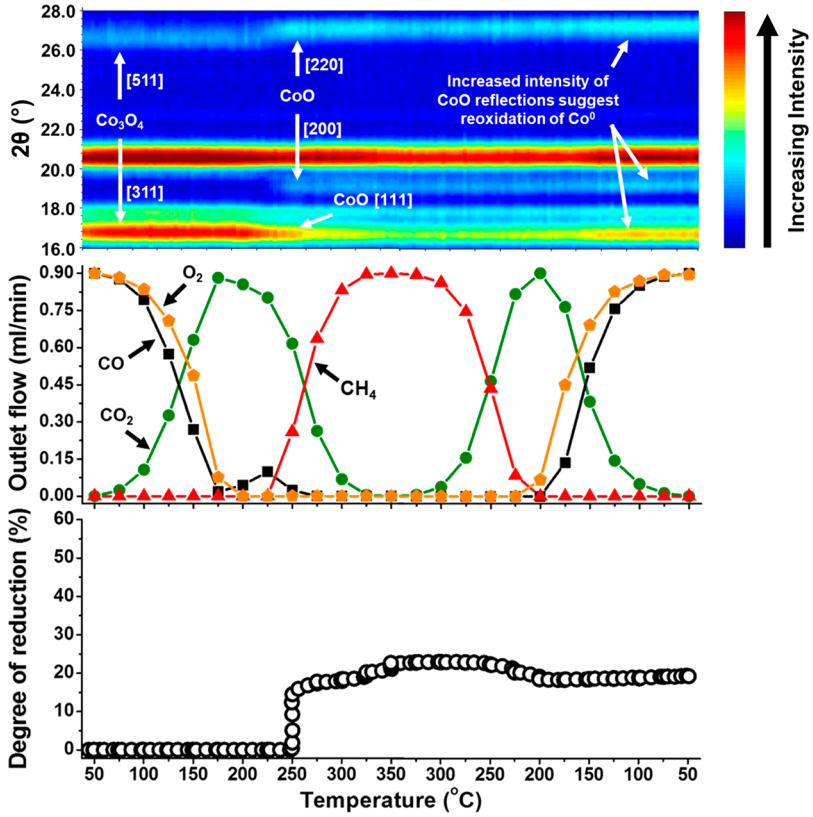

Figure 4. (Top) On-top view of the PXRD patterns recorded for CAT 1 (radiation source: Mo Kα1 = 0.7093 Å). (Middle) Measured outlet flow rates of CO, O_2, CO_2, and CH_4. (Bottom) Changes in the degree of reduction calculated from the magnetometer-derived data. The PXRD reflections for Co_3O_4 and CoO were assigned using the ICDD card nos.: 01-073-1701 and 00-043-1004, respectively.

Supporting Information. The catalyst CAT 1 exhibits superior CO oxidation activity below 225 °C, reaching higher CO_2 yields than CAT 2 at all temperatures and achieving the highest yield (98%) at a temperature of 175 °C. The weak

DOI: 10.1021/acscatal.9b00685
ACS Catal. 2019, 9, 7166−7178

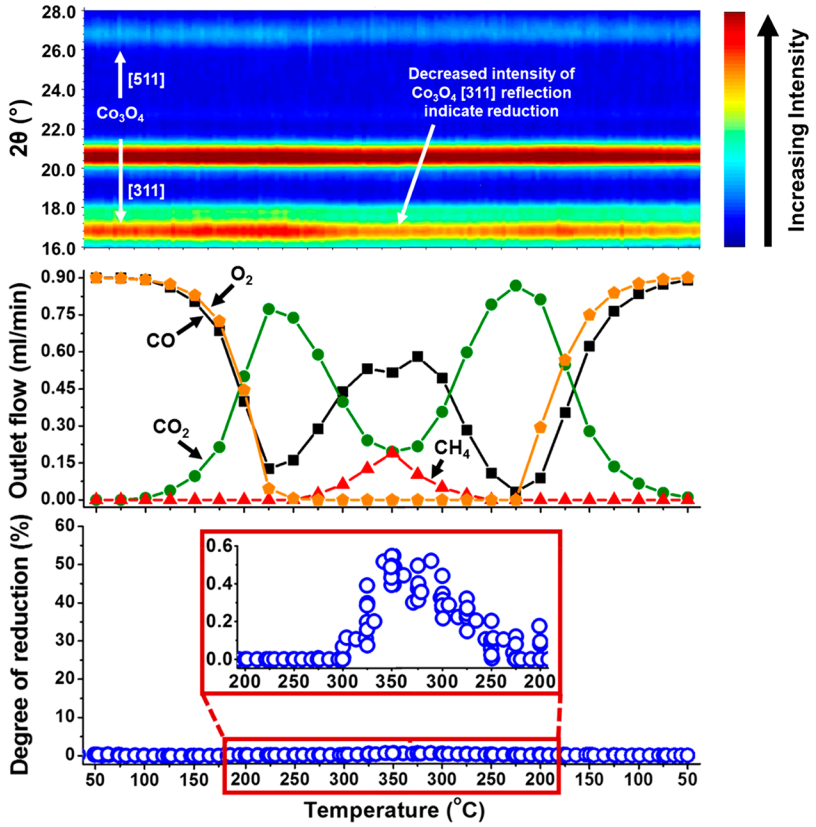

Figure 5. (Top) On-top view of the PXRD patterns recorded for CAT 2 (radiation source: Mo Kα1 = 0.7093 Å). (Middle) Measured outlet flow rates of CO, O_2, CO_2, and CH_4. (Bottom) Changes in the degree of reduction calculated from the magnetometer-derived data. Also shown is a magnified region of the degree of reduction plot (from 200 °C (heating) to 200 °C (cooling)).

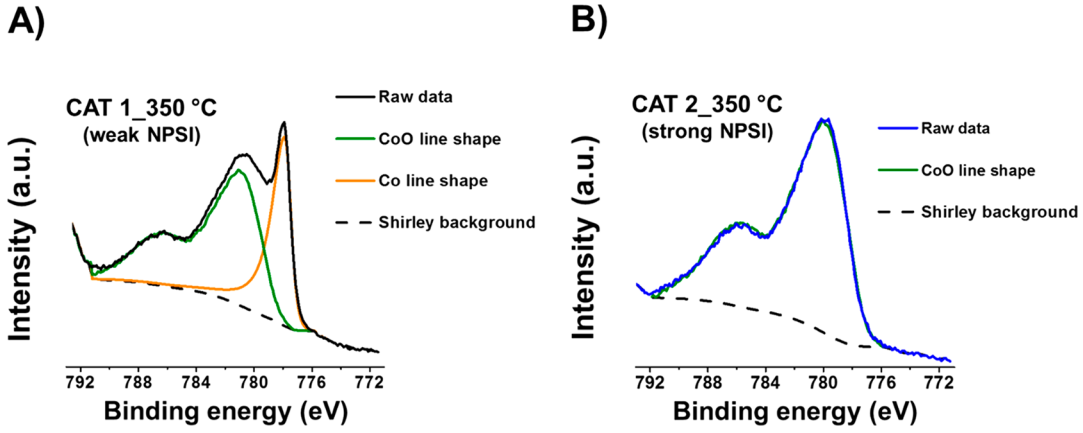

Figure 6. Recorded Co 2p core level spectra of (A) CAT 1 and (B) CAT 2 after being exposed to dry CO-PrOx conditions at 350 °C.

NPSI in CAT 1 are thought to be advantageous in that a higher amount (or surface area) of the active Co_3O_4 sites is made available to the gas reactants instead of strongly interacting with the support. Also, according to most literature, CO oxidation over Co_3O_4 is believed to proceed via the Mars–van Krevelen (MvK) mechanism,[13−16,37,38] which requires the Co_3O_4 surface to be redox active. Therefore, the high activity of CAT 1 can also be attributed to the facile reducibility of the (surface) oxide phase.

The co-fed O_2 is also consumed in each reaction, with CAT 1 reaching complete O_2 conversion at 200 °C and CAT 2 achieving a similar conversion at 250 °C. Although complete O_2 conversion is reached at these temperatures, the yields of CO_2 are seen to decrease above 225 °C. This is an indication of a loss in O_2 selectivity to CO_2 because of the competing H_2 oxidation reaction, which has proven to be unavoidable even over other catalysts, especially when O_2 is fed in excess of the stoichiometric amount (see section 2.3.2).[8−13,15,16,36,39−41] In addition, CAT 1 reduces from Co_3O_4 to CoO at 225 °C according to PXRD and to metallic Co at 250 °C as measured in the magnetometer. Concurrent with the formation of metallic Co is the undesired formation of CH_4, which also competes with the CO oxidation reaction.[8,9,36,40,41] We note that the metallic Co phase in CAT 1 is not observed in PXRD because of the overlap between the expected fcc Co [111] reflection at 20.0° and the alumina [400] reflection at 20.7°.

DOI: 10.1021/acscatal.9b00685
ACS Catal. 2019, 9, 7166−7178

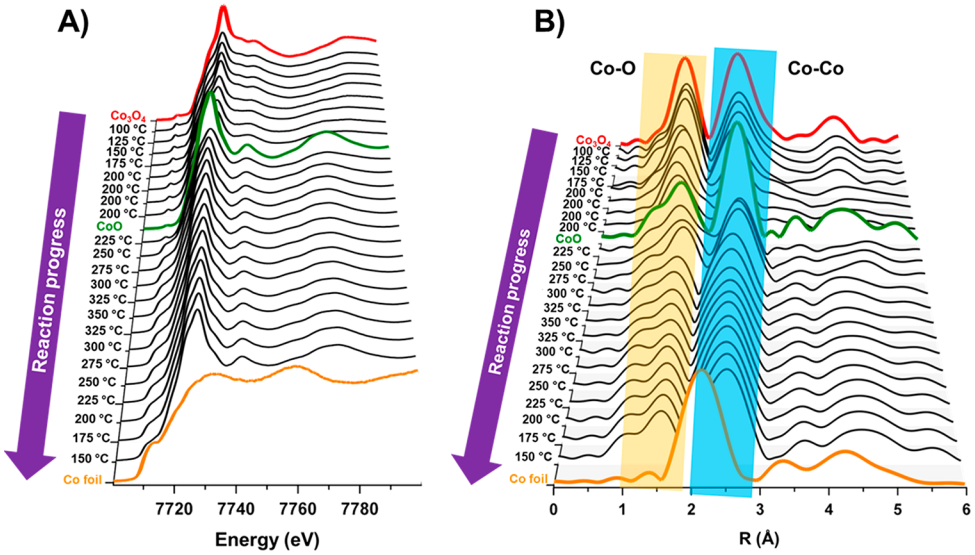

Figure 7. (A) Normalized XANES spectra and (B) the k^2-weighted Fourier transform of the EXAFS data of the CAT 1 sample during dry CO-PrOx. The reference spectra of Co_3O_4, CoO, and Co foil are also included. Preparation methods for Co_3O_4 and CoO can be found in ref 44.

We also note that at 350 °C, the calculated degree of reduction of Co_3O_4 to metallic Co from the magnetometry data is 22%, which is equivalent to 1.6 wt % of metallic Co (and 7.4 wt % CoO) in the entire supported sample. This low weight fraction of the metal in conjunction with the expected small crystallite size is close to the detection limit of laboratory-based PXRD.

For CAT 2, neither CoO nor metallic Co are observed in PXRD, but the decrease in the intensity of the Co_3O_4 [311] reflection between 250 and 275 °C suggests that this catalyst was also partially reduced. The magnetometer estimated a very low degree of reduction to metallic Co for CAT 2 (less than 1%), which further supports the previously observed and discussed low reducibility in section 3.2. Although a low degree of reduction and a low yield of CH_4 (21%) is achieved by CAT 2, the amount of CO exiting the reactor increases with increasing temperature, which is undesired for H_2 fuel cell applications. This increasing exit of CO indicates that H_2 oxidation is favored over the CO oxidation pathway at elevated temperatures, seeing that O_2 is depleted above 250 °C.

Quasi-in-situ XPS was performed after exposing each catalyst to dry CO-PrOx conditions at 350 °C in the previously described "flow-over" cell. Figure 6 shows the Co 2p core-level spectra of CAT 1 and CAT 2. At 350 °C CAT 1 contains both CoO and metallic Co at a ratio of 66:34, while in CAT 2 only the CoO phase is detected (see Figure 6). Despite the XPS estimating a slightly higher relative metallic Co content than the magnetometer [a result of the differences in their reactor and gas flow systems, as well as their depth profile, i.e., bulk sensitivity (magnetometry) versus surface sensitivity (XPS)], the trends in the captured reduction behavior remain highly comparable.

When cooling the reactor below 350 °C, both catalysts gradually recover their CO oxidation activity as CO hydrogenation and H_2 oxidation diminish.[9,41] Surprisingly, the catalysts achieve higher CO_2 yields (at 225 °C in the case of CAT 2 and 200 °C in the case of CAT 1) compared to the yields achieved during the heating steps. According to the magnetometry data, the amount of metallic Co eventually decreases, which implies reoxidation of the catalysts. In CAT 2, there is complete disappearance of the metallic phase at 225 °C, while in CAT 1, the degree of reduction decreases from 22 to 19% at 200 °C and stays constant until 50 °C. We consider that complete reoxidation of metallic Co was not achieved because of the high overall H_2:O_2 partial pressure ratio and perhaps also kinetically hindered due to the stepwise decrease in temperature from 350 to 50 °C.

PXRD shows the presence of CoO during cooling in CAT 1 but no evidence of Co_3O_4 and remains inconclusive in terms of the presence of these oxides in CAT 2. Nonetheless, it is possible that the surfaces of these catalysts may contain the active Co^{3+}−Co^{2+} redox pair required for the oxidation of CO, which would explain the recovery of the activity upon cooling. In addition to surface and/or bulk reoxidation, the decreasing temperature may be kinetically favoring the oxidation of CO over methanation and H_2 oxidation.

From the PXRD, magnetometry, and XPS studies, the effect of employing different supporting methods is shown as both catalysts display clear differences in terms of their CO oxidation activity and Co_3O_4 phase stability. The catalyst CAT 2, with very strong NPSI, exhibited greater resistance to reduction (as also observed during H_2-TPR) but was less active than CAT 1 before any detectable phase changes could occur. The low CO oxidation activity of CAT 2 is possibly a consequence of having low amounts of surface Co_3O_4 sites (or area) available and very low (surface) reducibility because of the strong NPSI. Therefore, these studies so far have highlighted the advantages and disadvantages of either having a highly reducible catalyst or an almost irreducible one.

Due to the small crystallite sizes and low mass fractions of Co_3O_4 (especially in CAT 2), adequate characterization of the catalysts was challenging. Furthermore, quantification of the oxide phases was not possible from the PXRD patterns. Therefore, X-ray absorption spectroscopy (XAS) was employed to further study the catalysts during dry CO-PrOx conditions. This technique enables the analysis of amorphous and crystalline bulk materials with different magnetic properties (e.g., Co^0, CoO, and Co_3O_4). As PXRD, magnetometry, and XAS are bulk techniques and full in situ or operando XPS experiments could not be performed, the XAS studies were coupled with surface-sensitive diffuse reflectance infrared

DOI: 10.1021/acscatal.9b00685
ACS Catal. 2019, 9, 7166−7178

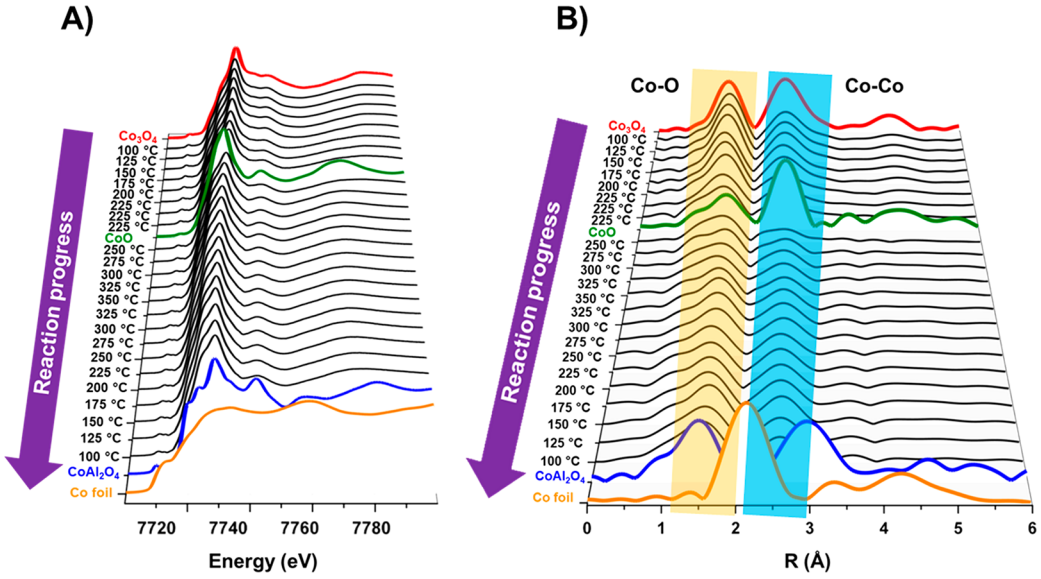

Figure 8. (A) Normalized XANES spectra and (B) the k^2-weighted Fourier transform of the EXAFS data of the CAT 2 sample during dry CO-PrOx. The reference spectra of Co_3O_4, CoO, $CoAl_2O_4$, and Co foil are also included. The preparation method for $CoAl_2O_4$ can be found in ref 45.

Fourier-transform spectroscopy (DRIFTS). DRIFTS would reveal the different adsorbed surface and gas-phase species present as a function of reaction conditions, which could in turn inform on the type of cobalt (oxide) surface formed.

3.3.2. Combined XAS/DRIFTS. Combined XAS/DRIFTS studies were performed on both catalysts, ramping under the CO-PrOx reaction gas in a stepwise manner similar to the PXRD and magnetometry studies. The X-ray absorption near edge structure (XANES) spectra of the fresh CAT 1 sample (i.e., between 50 and 175 °C) are consistent with cobalt being predominantly in the form of Co_3O_4. From 200 °C the main edge shifts to lower energy with the spectra resembling a mixture of CoO and Co between 250 and 350 °C. The presence of CoO is observed from the main feature after the edge shifting from 7729 to 7726 eV,[42,43] and the slight increase in the feature at 7709 eV is consistent with the formation of metallic Co[42,43] in Figure 7A. A linear combination fit of the XANES data (Figure S7A, SI) suggests that approximately 30% of the Co is present as Co^0, consistent with the 34 and 22% Co^0 estimated from the XPS and magnetometry results, respectively, with the remaining 70% cobalt in the form of CoO. Again, differences in the hydrodynamics of the utilized sample presentation devices are expected to result in minor composition differences. However, from the Fourier transform of the EXAFS data in Figure 7B, there is no evidence of metallic features, which, as with the PXRD, could be due to the presence of very small Co^0 clusters and/or not bulk-like Co^0.

The fresh CAT 2 sample also resembles Co_3O_4 below 200 °C, similar to CAT 1. Above this temperature, the XANES spectra indicate a transformation to CoO, with a shift in the main edge toward lower energy and the main feature after the edge moving toward 7726 eV (Figure 8A). Unlike the CAT 1 sample, no evidence of Co^0 is observed from the XANES spectra or from the k^2-weighted Fourier transform of the EXAFS data (Figure 8B), which agrees with the PXRD and XPS studies as well as the catalytic performance data, where only limited amounts of CH_4 (less than 20% yield) were formed. A linear combination fit of the XANES spectra (Figure S7B, SI) suggests that at 350 °C the catalyst contains approximately 20% Co_3O_4 and 80% CoO. However, the magnetometer, the most sensitive technique for the detection of metallic cobalt under the given reaction conditions and sample presentation devices, detected small amounts of metallic Co, corresponding to a degree of reduction of under 1%.

The XANES spectra of CAT 2 shown in Figure 8A from 225 to 350 °C and back to 100 °C exhibit a feature at 7711 eV (also see Figure 9, which highlights this feature at selected

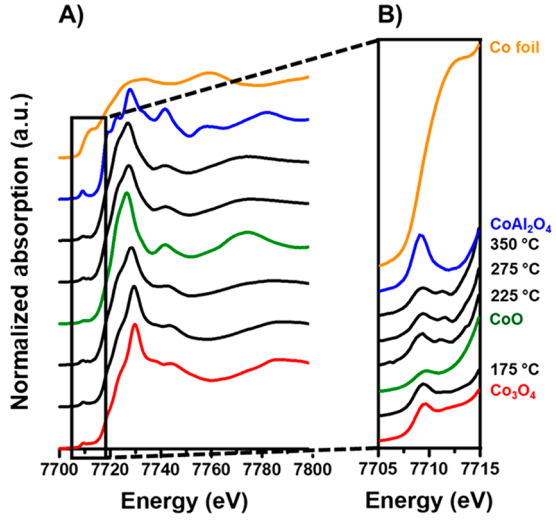

Figure 9. (A) Normalized XANES spectra at selected reaction temperatures upon heating and (B) a magnified region of the XANES spectra (between 7705 and 7715 eV) recorded during CO-PrOx over CAT 2. The reference spectra of Co_3O_4, CoO, $CoAl_2O_4$, and Co foil and are also included.

temperatures) not previously observed in the XANES spectra of CAT 1. This feature appears to closely coincide with the metallic Co pre-edge feature at 7709 eV. However, the assignment of this feature to Co^0 may not be accurate, as the magnetometry and gas chromatography results only show the formation of Co^0 and CH_4, respectively, at much higher reaction temperatures (above 225 °C). Referencing to the pre-

DOI: 10.1021/acscatal.9b00685
ACS Catal. 2019, 9, 7166−7178

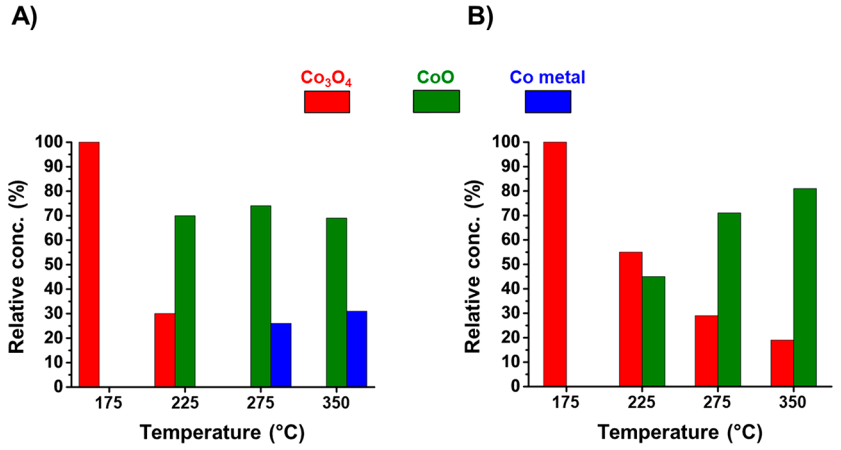

Figure 10. Results from the linear combination fit of the XANES at selected temperatures during heating for (A) CAT 1 and (B) CAT 2.

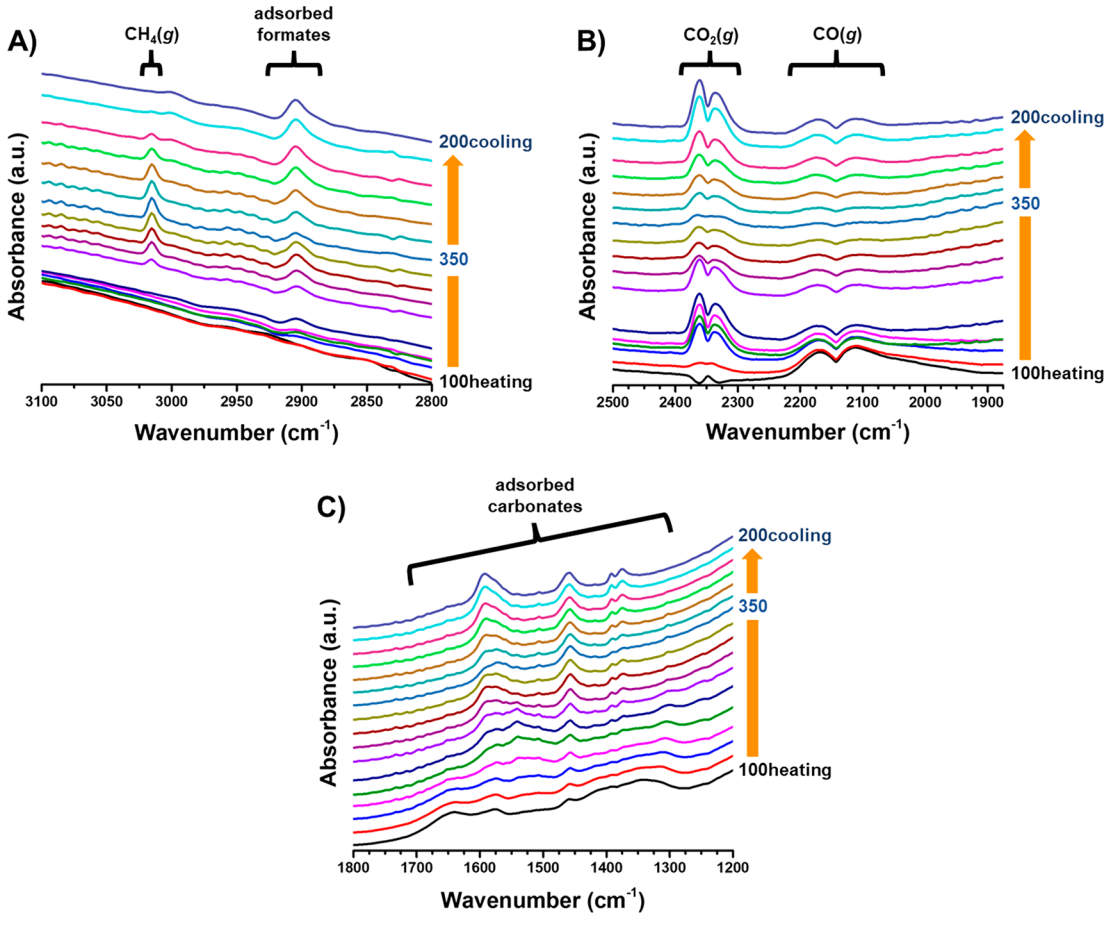

Figure 11. DRIFTS spectra collected during the CO-PrOx reaction over the CAT 1 sample showing the (A) CH_4(g) and formate and (B) CO_2(g) and CO(g), as well as the (C) carbonates region.

edge of $CoAl_2O_4$ seems to also rule out the presence of this mixed metal oxide as being the feature at 7711 eV.

At this stage, without any evidence from the literature, it is thought that the feature at 7711 eV may be some other $Co_xAl_yO_z$ species which differs from the bulk $CoAl_2O_4$. From the H_2-TPR results there are Co-based species (either formed during calcination or H_2-TPR) in CAT 2 requiring temperatures above 750 °C to reduce, and such reduction behavior is commonly associated with cobalt aluminate-like species ($Co_xAl_yO_z$) in Co_3O_4/Al_2O_3 (or Co/Al_2O_3).[5−7,34] Furthermore, Tsakoumi et al.[46] proposed that Co particles smaller than 5.3 nm may form such species at the nanoparticle−support interface after reduction in H_2. Therefore, it is possible that, during CO-PrOx, CAT 2 forms small amounts of $Co_xAl_yO_z$ that remain stable above 225 °C and even upon cooling back to 100 °C.

Despite the presence of an unknown $Co_xAl_yO_z$ phase, Figure 10 shows the results from the LCF performed at selected temperatures during heating for both catalysts assuming the presence of Co_3O_4, CoO, and metallic Co only. It can be seen

DOI: 10.1021/acscatal.9b00685
ACS Catal. 2019, 9, 7166−7178

that CAT 1 shows partial reduction to CoO and Co^0, which is consistent with the XPS, magnetometry, and PXRD studies. However, CAT 2 shows minimal reduction, only forming CoO in the XAS studies with small amounts of Co^0 only observed in the analysis of the magnetometry data.

Both surface-adsorbed species and gas-phase species were monitored using DRIFTS due to the geometry of the cell.[29−31] The formation of gas-phase CH_4 and CO_2 was monitored at temperatures consistent with the GC data shown in Figure 4 for CAT 1. The formation of CO_2 from the gas-phase bands at 2360 and 2335 cm^{-1} [8,40] in Figure 11B also follows the trend observed from the GC analysis during the operando magnetometry and PXRD experiments, reaching a maximum between 175 and 225 °C. The formation of CH_4 in the DRIFTS spectra at 3020 cm^{-1}[40] is recorded above 250 °C when heating and disappears below 250 °C when cooling (see Figure 11A), consistent with the formation and reoxidation of Co^0, respectively (see magnetometry and XAS results).

No adsorbed CO species were observed in the recorded spectra (even after subtracting the gas-phase CO band; see Figure S9) as the stretching modes of CO adsorbed on Co^0, Co^{2+}, and Co^{3+} are expected at 2023−2025, 2120−2170, and 2178−2180 cm^{-1}, respectively.[14,47] The absence of these bands agrees with previous studies, where only carbonate species (1700−1200 cm^{-1}) and possibly formates (2905 cm^{-1}) are reported during CO-PrOx.[8,14,16,40,48] It is possible that CO reacts rapidly on Co_3O_4 to form carbonates, as has been suggested in the literature.[16] The lack of CO adsorption bands on Co^0 could be due to the limited stability of these species under flowing gases, as these bands are reported to be easily removed on evacuation.[47]

Carbonate species are, however, observed under CO-PrOx conditions on CAT 1, as shown in Figure 11C. Monodentate carbonates are assigned to the bands at 1507, 1390, and 1375 cm^{-1},[16,48] which grow gradually during the reaction, even upon cooling. This gradual growth in concentration is also observed for the formates at 2905 cm^{-1}.[16,48] As these bands do not follow measured trends in the reactor outlet gas composition, we suggest that they may be spectator species. Bidentate carbonates (1540, 1249 cm^{-1})[16] are formed above 150 °C and increase in intensity up to 250 °C. This coincides with the temperature where CO_2 production reaches a maximum, indicating that these species may possibly be involved in the oxidation reaction.

Similar carbonates were also present in CAT 2 as the temperature was increased (see Figure S10A). However, we note that it is difficult to elucidate the kind of cobalt surface (i.e., if it is oxidic or metallic) onto which the carbonates are adsorbed, as their stability could be temperature-dependent and some may not necessarily partake in the reaction (e.g., monodentates in the present case). Furthermore, carbonates were also observed on bare Al_2O_3 under CO-PrOx conditions (Figure S10B), which implies that the formation and/or adsorption of these species is not limited to the cobalt surfaces only.

Therefore, only the bands for the gas-phase species and bidentate carbonates provide some information on the nature of the catalyst's surface at the different reaction temperatures (together with the data from XPS, PXRD, magnetometry, and XAS). However, the position at which the IR spectra were taken along the catalyst bed may have not been ideal, as there could be different surfaces exposed and, consequently, different species being adsorbed and detected. It may be helpful to perform spatially resolved DRIFTS (combined with XAS),[49] which might allow for the sample to be analyzed at different reactor positions and discriminate between different catalyst surfaces and surface-adsorbed species. Such an experiment could be performed over both unsupported and supported forms, respectively, of the catalyst to also investigate the support effect on the presence and/or adsorption of certain species.

4. CONCLUSIONS

The present study has addressed the challenges faced when using the transition-metal oxide Co_3O_4, regarding its catalytic performance and phase stability under the reducing environment of CO-PrOx. This was possible through the use of various in situ techniques that collectively provided very valuable insight into the effect of nanoparticle−support interaction (NPSI) on the performance and phase stability of Co_3O_4. Depending on the method of preparing the supported catalyst, the strength of the NPSI can be greatly affected. It was shown that first preparing calcined Co_3O_4 nanoparticles and then physically mixing these with the Al_2O_3 support in a liquid medium (as in CAT 1) result in weak NPSI, but contacting the support with $Co(NO_3)_2{\cdot}6H_2O$(aq) within a reverse microemulsion (as in CAT 2) gives a supported catalyst with much stronger NPSI. From the kinetic data obtained during the operando CO-PrOx experiments, weak NPSI favor high CO oxidation activity over unreduced Co_3O_4, while strong NPSI minimize Co_3O_4 reduction and the unwanted formation of CH_4 at elevated reaction temperatures. The observations from the in situ analysis and kinetic data suggest that significant stability of the active oxide phase is desired; however, the catalyst (surface) needs to be reducible to some extent, as this is a requirement for the oxidation of CO over metal oxides via the Mars−van Krevelen mechanism. Therefore, future work can focus on investigating either other support materials or (oxidation) promoters that can maximize both catalyst stability and activity.

■ ASSOCIATED CONTENT

Supporting Information

The Supporting Information is available free of charge on the ACS Publications website at DOI: 10.1021/acscatal.9b00685.

Text describing the concept of magnetism and magnetometer calibration, linear combinations of selected XANES spectra, and other DRIFTS data (PDF)

■ AUTHOR INFORMATION

Corresponding Author

*E-mail: michael.claeys@uct.ac.za.

ORCID

Emma K. Gibson: 0000-0002-7839-3786
Peter P. Wells: 0000-0002-0859-9172
Michael Claeys: 0000-0002-5797-5023

Notes

The authors declare no competing financial interest.

The raw data supporting this study are openly available from the University of Cape Town repository at DOI: 10.25375/uct.8332652.

DOI: 10.1021/acscatal.9b00685
ACS Catal. 2019, 9, 7166−7178

■ ACKNOWLEDGMENTS

The authors would like to acknowledge the financial support from Johnson Matthey, DST-NRF Centre of Excellence in Catalysis Research (*c**change), the Royal Society in the form of the Newton Advanced Fellowship program (NA140201, Phase transformations of nanoparticulate heterogeneous catalysts captured in situ) and the Economic and Social Research Council in the form of the Newton project for United Kingdom−South Africa Ph.D. exchanges. The UK Catalysis Hub is kindly thanked for resources and support provided via our membership of the UK Catalysis Hub Consortium and funded by EPSRC grant EP/R026815/1. In addition, they thank the team from the Centre of Imaging and Analysis based at the University of Cape Town (UCT) for their assistance with TEM and EDX and the team in the Analytical Laboratories of the Chemical Engineering Department at UCT for access to their H_2-TPR instrument. Ms. Ellie Dann from the UK Catalysis Hub is also thanked for assisting during the beamtime at the Diamond Light Source (session SP16006-1) on beamline B18. Lastly, the authors would like to relay their appreciation for the opportunity offered by Diamond Light Source to perform in situ XAS/DRIFTS and for the assistance offered by the B18 beamline scientist, Dr. Diego Gianolio.

■ REFERENCES

(1) Perego, C.; Villa, P. Catalyst Preparation Methods. *Catal. Today* **1997**, *34*, 281−305.
(2) Reuel, R. C.; Bartholomew, C. H. Effects of Support and Dispersion on the CO Hydrogenation Activity/Selectivity Properties of Cobalt. *J. Catal.* **1984**, *85*, 78−88.
(3) Ishihara, T.; Eguchi, K.; Arai, H. Importance of Surface Hydrogen Concentration in Enhancing Activity of Co-Ni Alloy Catalyst for CO Hydrogenation. *J. Mol. Catal.* **1992**, *72*, 253−261.
(4) Girardon, J.-S.; Lermontov, A. S.; Gengembre, L.; Chernavskii, P. A.; Griboval-Constant, A.; Khodakov, A. Y. Effect of Cobalt Precursor and Pretreatment Conditions on the Structure and Catalytic Performance of Cobalt Silica-Supported Fischer−Tropsch Catalysts. *J. Catal.* **2005**, *230*, 339−352.
(5) Fischer, N.; Minnermann, M.; Baeumer, M.; van Steen, E.; Claeys, M. Metal Support Interactions in Co_3O_4/Al_2O_3Catalysts Prepared from w/o Microemulsions. *Catal. Lett.* **2012**, *142*, 830−837.
(6) Jacobs, G.; Das, T. K.; Zhang, Y.; Li, J.; Racoillet, G.; Davis, B. H. 2002. Fischer−Tropsch Synthesis: Support, Loading, and Promoter Effects on the Reducibility of Cobalt Catalysts. *Appl. Catal., A* **2002**, *233*, 263−281.
(7) Storsæter, S.; Borg, Ø.; Blekkan, E. A.; Holmen, A. Study of the Effect of Water on Fischer−Tropsch Synthesis over Supported Cobalt Catalysts. *J. Catal.* **2005**, *231*, 405−419.
(8) Zhao, Z.; Yung, M.; Ozkan, U. S. Effect of Support on the Preferential Oxidation of CO Over Cobalt Catalysts. *Catal. Commun.* **2008**, *9*, 1465−1471.
(9) Nyathi, T. M.; Fischer, N.; York, A. P. E.; Claeys, M. Effect of Crystallite Size on the Performance and Phase Transformation of Co_3O_4/Al_2O_3Catalysts During CO-PrOx - An *In Situ* Study. *Faraday Discuss.* **2017**, *197*, 269−285.
(10) Oh, S. H.; Sinkevitch, R. M. Carbon Monoxide Removal from Hydrogen-Rich Fuel Cell Feedstreams by Selective Catalytic Oxidation. *J. Catal.* **1993**, *142*, 254−262.
(11) Edwards, N.; Ellis, S. R.; Frost, J. C.; Golunski, S. E.; van Keulen, A. N. J.; Lindewald, N. G.; Reinkingh, J. G. On-board Hydrogen Generation for Transport Applications: The Hotspot Methanol Processor. *J. Power Sources* **1998**, *71*, 123−128.
(12) Ghenciu, A. F. Review of Fuel Processing Catalysts for Hydrogen Production in PEM Fuel Cell Systems. *Curr. Opin. Solid State Mater. Sci.* **2002**, *6*, 389−399.
(13) Omata, K.; Takada, T.; Kasahara, S.; Yamada, M. Active Site of Substituted Cobalt Spinel Oxide for Selective Oxidation of CO/H_2: Part II. *Appl. Catal. A* **1996**, *146*, 255−267.
(14) Jansson, J.; Palmqvist, A. E. C.; Fridell, E.; Skoglundh, M.; Osterlund, L.; Thormahlen, P.; Langer, V. On the Catalytic Activity of Co_3O_4 in Low-Temperature CO Oxidation. *J. Catal.* **2002**, *211*, 387−397.
(15) Iablokov, V.; Barbosa, R.; Pollefeyt, G.; Van Driessche, I.; Chenakin, S.; Kruse, N. Catalytic CO Oxidation over Well-Defined Cobalt Oxide Nanoparticles: Size-Reactivity Correlation. *ACS Catal.* **2015**, *5*, 5714−5718.
(16) Lukashuk, L.; Yigit, N.; Rameshan, R.; Kolar, E.; Teschner, D.; Hävecker, M.; Knop-Gericke, A.; Schlögl, R.; Föttinger, K.; Rupprechter, G. *Operando*Insights into CO Oxidation on Cobalt Oxide Catalysts by NAP-XPS, FTIR and XRD. *ACS Catal.* **2018**, *8*, 8630−8641.
(17) Fischer, N.; van Steen, E.; Claeys, M. Preparation of Supported Nano-Sized Cobalt Oxide and FCC Cobalt Crystallites. *Catal. Today* **2011**, *171*, 174−179.
(18) ICDD. *PDF-2 Release 2008 (Database)*; Kabekkodu, S., Ed.; International Centre for Diffraction Data: Newtown Square, PA, 2008.
(19) Coelho, A. A. Indexing of Powder Diffraction Patterns by Iterative Use of Singular Value Decomposition. *J. Appl. Crystallogr.* **2003**, *36*, 86−95.
(20) Scarlett, N. V. Y.; Madsen, I. C. Quantification of Phases with Partial or No Known Crystal Structures. *Powder Diffr.* **2006**, *21*, 278−284.
(21) Rasband, W. *Image J. 1.51a*; National Institute of Mental Health: Bethesda, MD, 2016.
(22) Claeys, M.; van Steen, E.; Visagie, J. L.; van de Loosdrecht, J. Magnetometer. US Patent. 8,773,118 B2, 2014.
(23) Fischer, N.; Clapham, B.; Feltes, T.; van Steen, E.; Claeys, M. Size-Dependent Phase Transformation of Catalytically Active Nanoparticles Captured *In Situ*. *Angew. Chem., Int. Ed.* **2014**, *53*, 1342−1345.
(24) Claeys, M.; Fischer, N. Sample Presentation Device for Radiation-based Analytical Equipment. US Patent 8,597,598 B2, 2013.
(25) Fischer, N.; Claeys, M. Phase Changes Studied Under *In Situ* Conditions-A Novel Cell. *Catal. Today* **2016**, *275*, 149−154.
(26) Buschow, K. H. J. *Encyclopedia of Materials: Science and Technology*; Elsevier: Amsterdam, Netherlands, 2001.
(27) Mousavand, T.; Naka, T.; Sato, K.; Ohara, S.; Umetsu, M.; Takami, S.; Nakane, T.; Matsushita, A.; Adschiri, T. Crystal Size and Magnetic Field Effects in Co_3O_4Antiferromagnetic Nanocrystals. *Phys. Rev. B: Condens. Matter Mater. Phys.* **2009**, *79*, No. 144411.
(28) Kittel, C. *Introduction to Solid State Physics*; John Wiley & Sons, Inc.: London, 2009.
(29) Marinkovic, N. S.; Wang, Q.; Barrio, L.; Ehrlich, S. N.; Khalid, S.; Cooper, C.; Frenkel, A. I. Combined *In Situ*X-ray Absorption and Diffuse Reflectance Infrared Spectroscopy: An Attractive Tool for Catalytic Investigations. *Nucl. Instrum. Methods Phys. Res., Sect. A* **2011**, *649*, 204−206.
(30) Gibson, E. K.; Beale, A. M.; Catlow, C. R. A.; Chutia, A.; Gianolio, D.; Gould, A.; Kroner, A.; Mohammed, K. M. H.; Perdjon, M.; Rogers, S. M.; Wells, P. P. Restructuring of AuPd Nanoparticles Studied by a Combined XAFS/DRIFTS Approach. *Chem. Mater.* **2015**, *27*, 3714−3720.
(31) Dann, E. K.; Gibson, E. K.; Catlow, C. R. A.; Collier, P.; Eralp Erden, T. E.; Gianolio, D.; Hardacre, C.; Kroner, A.; Raj, A.; Goguet, A.; Wells, P. P. Combined *In Situ*XAFS/DRIFTS Studies of the Evolution of Nanoparticle Structures from Molecular Precursors. *Chem. Mater.* **2017**, *29*, 7515−7523.
(32) Newville, M. IFEFFIT: Interactive XAFS Analysis and FEFF Fitting. *J. Synchrotron Radiat.* **2001**, *8*, 322−324.
(33) Ravel, B.; Newville, M. ATHENA, ARTEMIS, HEPHAESTUS: Data Analysis for X-ray Absorption Spectroscopy using IFEFFIT. *J. Synchrotron Radiat.* **2005**, *12*, 537−541.

DOI: 10.1021/acscatal.9b00685
ACS Catal. 2019, 9, 7166−7178

(34) Sirijaruphan, A.; Horvath, A.; Goodwin, J. G., Jr.; Oukaci, R. Cobalt Aluminate Formation in Alumina-Supported Cobalt Catalysts: Effects of Cobalt Reduction State and Water Vapour. *Catal. Lett.* **2003**, *91*, 89−94.
(35) Biesinger, M. C.; Payne, B. P.; Grosvenor, A. P.; Lau, L. W. M.; Gerson, A. R.; Smart, R. St. C. Resolving Surface Chemical States in XPS Analysis of First Row Transition Metals, Oxides and Hydroxides: Cr, Mn, Fe, Co and Ni. *Appl. Surf. Sci.* **2011**, *257*, 2717−2730.
(36) Lukashuk, L.; Föttinger, K.; Kolar, E.; Rameshan, C.; Teschner, D.; Hävecker, M.; Knop-Gericke, A.; Yigit, N.; Li, H.; McDermott, E.; Stöger-Pollach, M.; Rupprechter, G. *Operando* XAS and NAP-XPS Studies of Preferential CO Oxidation on Co_3O_4 and CeO_2-Co_3O_4Catalysts. *J. Catal.* **2016**, *344*, 1−15.
(37) Mars, P.; van Krevelen, D. W. Oxidations Carried Out by Means of Vanadium Oxide Catalysts. *Chem. Eng. Sci.* **1954**, *3*, 41−59.
(38) Perti, D.; Kabel, R. L.; McCarthy, G. J. Kinetics of CO Oxidation Over Co_3O_4/γ-Al_2O_3. *AIChE J.* **1985**, *31*, 1435−1440.
(39) Teng, Y.; Sakurai, H.; Ueda, A.; Kobayashi, T. Oxidative Removal of CO in Hydrogen by Using Metal Oxide Catalysts. *Int. J. Hydrog. Energy* **1999**, *24*, 355−358.
(40) Yung, M. M.; Zhao, Z.; Woods, M. P.; Ozkan, U. S. Preferential Oxidation of Carbon Monoxide on CoO_x/ZrO_2. *J. Mol. Catal. A: Chem.* **2008**, *279*, 1−9.
(41) Khasu, M.; Nyathi, T.; Morgan, D. J.; Hutchings, G. J.; Claeys, M.; Fischer, N. Co_3O_4Morphology in the Preferential Oxidation of CO. *Catal. Sci. Technol.* **2017**, *7*, 4806−4817.
(42) Moen, A.; Nicholson, D. G.; Clausen, B. S.; Hansen, P. L.; Molenbroek, A.; Steffensen, G. X-ray Absorption Spectroscopic Studies at the Cobalt K-Edge on a Reduced Al_2O_3-Supported Rhenium-Promoted Cobalt Fischer−Tropsch Catalyst. *Chem. Mater.* **1997**, *9*, 1241−1247.
(43) Ernst, B.; Bensaddik, A.; Hilaire, L.; Chaumette, P.; Kiennemann, A. Study on a Cobalt Silica Catalyst During Reduction and Fischer−Tropsch Reaction: *In Situ*EXAFS Compared to XPS and XRD. *Catal. Today* **1998**, *39*, 329−341.
(44) Wolf, M.; Fischer, N.; Claeys, M. Surfactant-Free Synthesis of Monodisperse Cobalt Oxide Nanoparticles of Tunable Size and Oxidation State Developed by Factorial Design. *Mater. Chem. Phys.* **2018**, *213*, 305−312.
(45) Karmaoui, M.; Silva, N. J. O.; Amaral, V. S.; Ibarra, A.; Millán, Á.; Palacio, F. Synthesis of Cobalt Aluminate Nanopigments by a Non-Aqueous Sol-Gel Route. *Nanoscale* **2013**, *5*, 4277−4283.
(46) Tsakoumis, N. E.; Walmsley, J. C.; Rønning, M.; van Beek, W.; Rytter, E.; Holmen, A. Evaluation of Reoxidation Thresholds for γ-Al_2O_3-Supported Cobalt Catalysts Under Fischer−Tropsch Synthesis Conditions. *J. Am. Chem. Soc.* **2017**, *139*, 3706−3715.
(47) Hadjiivanov, K. I.; Vayssilov, G. N. Characterization of Oxide Surfaces and Zeolites by Carbon Monoxide as an IR Probe Molecule. *Adv. Catal.* **2002**, *47*, 307−511.
(48) Marbán, G.; López, I.; Valdés-Solís, T. Preferential Oxidation of CO by CuO_x/CeO_2Nanocatalysts Prepared by SACOP: Mechanisms of Deactivation Under the Reactant Stream. *Appl. Catal., A* **2009**, *361*, 160−169.
(49) Morgan, K.; Touitou, J.; Choi, J.-S.; Coney, C.; Hardacre, C.; Pihl, J. A.; Stere, C. E.; Kim, M.-Y.; Stewart, C.; Goguet, A.; Partridge, W. P. Evolution and Enabling Capabilities of Spatially Resolved Techniques for the Characterization of Heterogeneously Catalyzed Reactions. *ACS Catal.* **2016**, *6*, 1356−1381.

DOI: 10.1021/acscatal.9b00685
ACS Catal. 2019, 9, 7166−7178